Chapter

Linear Switched Reluctance Motors

Jordi Garcia-Amoros, Pere Andrada and Baldui Blanque

Abstract

This chapter deals with linear switched reluctance machines (LSRMs). Linear switched reluctance machines are the counterpart of the rotary switched reluctance machine (SRM), and now they have aroused great interest in the field of electrical machines and drives. In this chapter, first, a mathematical model is presented, and then a procedure for the design of this kind of machines is proposed. Next, a linear switched reluctance force actuator, based on the before designed procedure, is simulated. In addition, experimental proofs of the goodness of the design process and of the accuracy of the simulation of the linear switched reluctance force actuator are given.

Keywords: linear switched reluctance machines (LSRMs), mathematical model, finite element analysis (FEA), design procedure, simulation

1. Introduction

Nowadays, there is a great interest in linear electric machines and especially in linear switched reluctance machines (LSRMs). LSRMs are an attractive alternative to permanent magnet linear motors (PMLM), despite the fact that the force/volume ratio is about 60% lower for LSRMs [1]. On the other hand, the absence of permanent magnet makes them less expensive and easy to assemble and provides a greater robustness and a good fault tolerance capability. LSRMs have been proposed for a wide range of applications such as precise motion control [2], propulsion railway transportation systems [3], vertical translation [4], active vehicle's suspension system [5], life-support applications [6], and in direct-drive wave energy conversion [7].

The LSRMs consist of two parts: the active part or primary part and the passive or secondary. The active part contains the windings and defines two main types of LSRMs: transverse and longitudinal. It is longitudinal when the plane that contains the flux lines is parallel to the line of movement and transverse when it is perpendicular. Other classifications are considering the windings totally concentrated in one coil per phase [2] or partially concentrated in two poles per phase (i.e., single-sided) or four poles per phase (double-sided) [3, 4]. **Figure 1** shows all the possible configurations belonging to this classification. The simplest structure is the single-sided flat LSRM shown in **Figure 1a**, in which the number of stator active poles is $2 \cdot m$, and the number of poles per phase (N_{pp}) is 2. A conventional double-sided flat LSRM (see **Figure 1b**) is created by joining two single-sided structures; in this case $N_{pp} = 4$ and the number of stator active poles is $N_p = N_{pp} \cdot m$, where m is the number of phases. The double-sided structure (**Figure 1b** and **c**) balances the normal force over the mover, and therefore, the linear bearing does not have to support it. This

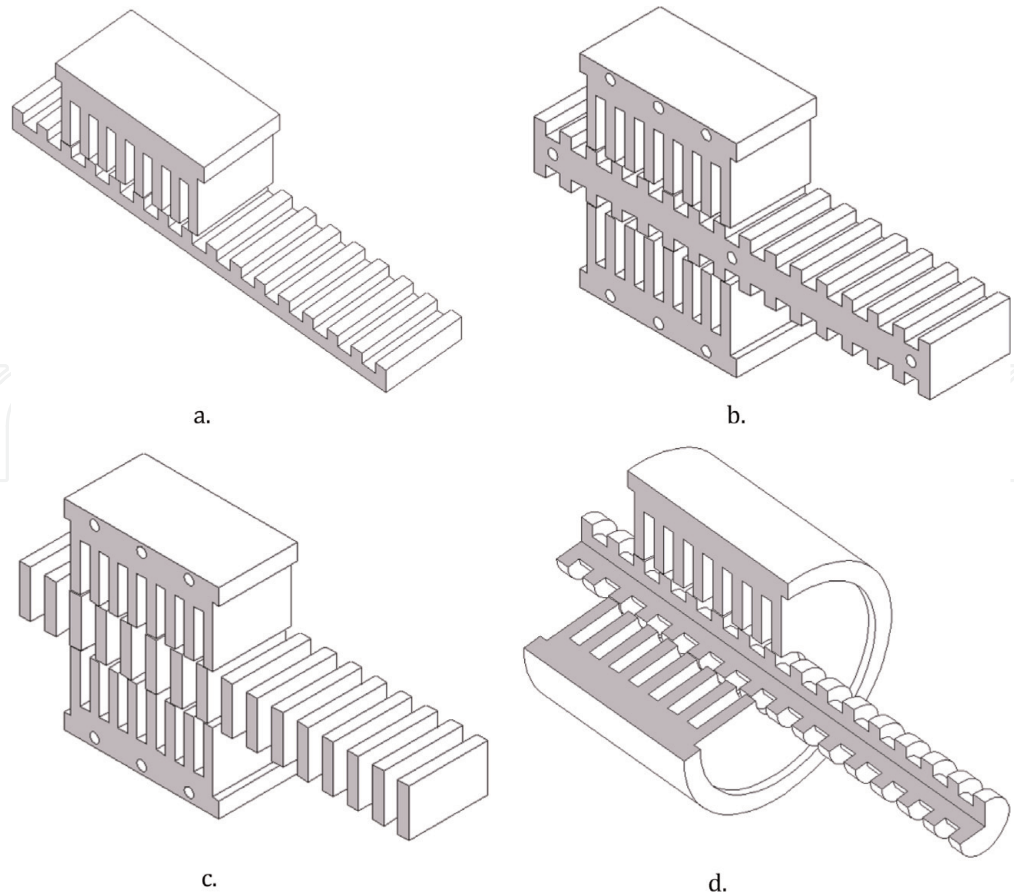

Figure 1.
Longitudinal flux LSRM topologies. (a) Single-sided; (b) conventional double-sided; (c) modified double-sided; and (d) tubular.

configuration has twice air gaps and coils than single-sided, which means a double translation force. Conventional double-sided (**Figure 1b**) can operate with one flux loop or two flux loops due to the magnetic connection between secondary poles. In the modified double-sided LSRM (**Figure 1c**), the secondary, the mover, is comprised of rectangular poles without connecting iron yokes between them but are mechanically joined by nonmagnetic mounting parts [8]. This arrangement reduces the mass of the mover, giving a higher translation force/mass ratio than conventional double-sided flat LSRM, which reduce the mover weight and its inertia although only allows operating with one flux loop. The tubular structure is shown in **Figure 1d**.

It is important to note that in an LSRM, thrust or translation force is produced by the tendency of its secondary or mover to translate to a position where the inductance of the excited phase is maximized, i.e., to reach the alignment of primary and secondary poles. Therefore, as in its rotary counterpart (SRM), a power converter with solid-state switches, usually an asymmetric bridge (with two switches and two diodes per phase), is needed to generate the right sequence of phase commutation. Thus, it is necessary to know, in every instant, the position of the secondary part or mover, for which a linear encoder is generally used.

2. Mathematical model of LSRM

The mathematical model of the LSRM consists on the voltage phase equation, the internal electromechanical force, and the mechanical equation, balance between internal electromagnetic force and load, friction, and dynamic forces.

DOI: http://dx.doi.org/10.5772/intechopen.89166

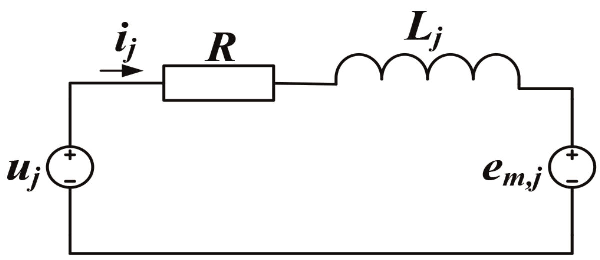

Figure 2.
Single-phase equivalent electric circuit of an LSRM.

The voltage equation of j-phase is equal to the resistive voltage drop plus the partial derivative of the j-phase flux-linkage respect time. This equation that can be written as (1) where in its second member the first term is the resistive voltage drop, the second term involves the voltage induced by the current variation, and the third is the induced voltage due to the relative movement of the primary and secondary parts at the speed u_b:

$$u_j = R \cdot i_j + \frac{\partial \psi_j(x, i)}{\partial i} \cdot \frac{di}{dt} + u_b \cdot \frac{\partial \psi_j(x, i)}{\partial x} \tag{1}$$

The respective derivatives in x (position) and i (current) of the *phase*-flux linkage $\left(\psi_j\right)$ give the j-phase incremental inductance, L_j (2), and the j-phase back electromotive force, $e_{m,j}$ (3).

$$L_j = \frac{\partial \psi_j(x, i)}{\partial i} \tag{2}$$

$$e_{m,j} = u_b \cdot \frac{\partial \psi_j(x, i)}{\partial x} \tag{3}$$

Rewriting (1)

$$u_j = R \cdot i_j + L_j \cdot \frac{di_j}{dx} + e_{m,j} \tag{4}$$

Then, the electrical equivalent circuit per phase of the LSRM is shown in **Figure 2**.

The total internal electromagnetic force (F_X) summing the force contribution of each phase is given by

$$F_X = \sum_{j=1}^{m} \left(\frac{\partial}{\partial x} \left(\int_0^I \psi_j(x, i) \cdot di \right) \bigg|_{I=ctn} \right) \tag{5}$$

The total internal electromagnetic force (5) is balanced by the dynamic force, product of mass by the acceleration, the friction force, and the applied mechanical load:

$$F_X = M \cdot \frac{du_b}{dt} + F_r + F_L \tag{6}$$

Rearranging Eqs. (1) and (6), we obtain the state-space equations (7), which define the dynamical model of an LSRM per phase:

$$\left.\begin{aligned} I_j &= \int \frac{1}{\dfrac{\partial \psi_j(x, i_j)}{\partial i_j}} \cdot \left(u_j - R.i_j - \frac{\partial \psi_j(x, i_j)}{\partial x} \cdot u_b \right) \cdot dt \\ u_b &= \int \frac{1}{M} \cdot (F_X - F_L - F_r) \cdot dt \end{aligned}\right\} \tag{7}$$

The simulation of the dynamic mathematical model (7) requires the flux-linkage characteristics $\psi_j(x, i)$ (see **Figure 3a**) and its partial derivatives $\frac{\partial \psi_j}{\partial i}$ (see **Figure 3c**) and $\frac{\partial \psi_j}{\partial x}$ (see **Figure 3d**), as well as the internal electromagnetic force F_X (see **Figure 3b**), whose values are obtained from FEM analysis.

3. LSRM design procedure

The design of electric rotating motors usually starts with the output equation. This equation relates the main dimensions (bore diameter and length), magnetic loading, and electric loading to the torque output. In this case, it introduced a similar development for the output equation of LSRM, in which the average translation force (output equation) depends on geometric parameters, magnetic loading, and current density [9].

Although the present study is focused in the longitudinal double-sided LSRM and the longitudinal modified double-sided LSRM (**Figure 1b** and **c**), the main dimensions describing its geometry are the same to that single-sided LSRM shown in **Figure 4**.

3.1 Design specification

The first step is to define the design specifications. These specifications affect not only the electromagnetic structure but also the power converter and the control

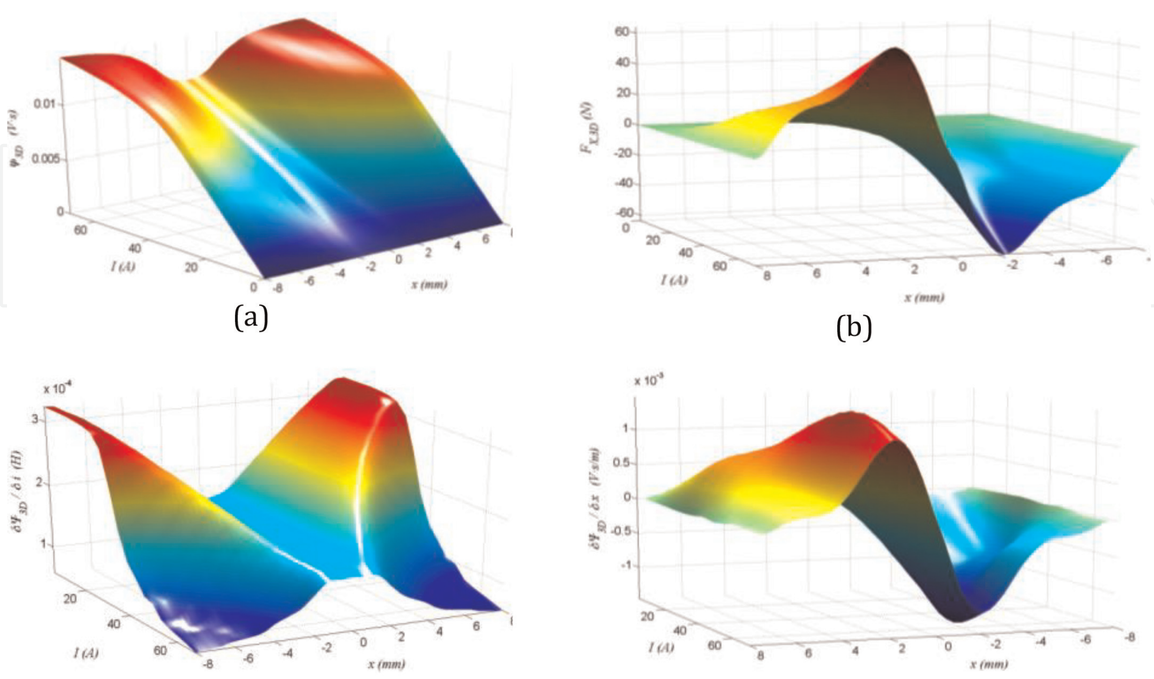

Figure 3.
FEM results plots for position x∈[−8,8] mm and current I∈[0,69] A. (a) Flux-linkage. (b) Internal electromagnetic force. (c) Partial derivative of flux-linkage with respect to current. (d) Partial derivative of flux-linkage with respect to position.

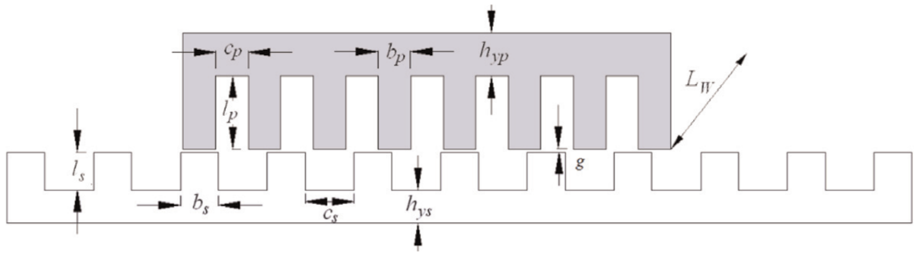

Figure 4.
Single-sided LSRM main dimensions.

Requirements	Constraints
• LSRM type • Power converter topology • Control strategy • Translation force (F_x) • Velocity (u_b) • Acceleration/deceleration (a) • Thermal duty cycle • Number of phases (m) • Pole Stroke (PS) • Mover stroke (TS)	• DC bus voltage (V_b) • Magnetic material • Temperature rise • Some critical dimensions (i.e., air-gap length)

Table 1.
Requirements and constrains.

strategy. They are also different in nature (mechanical, electrical, thermal) and can be classified into two general areas, requirements and constraints; the most usual are listed in **Table 1**.

Figure 5 shows a flowchart with the different steps of the design process [9]. These steps begin with the definition of the specifications. Then, the main dimensions are obtained using the output equation. In the next step, the number of turns and the wire gauge are determined following an internal iterative process. Then a first performance FEM-computation is performed. Finite element analysis and thermal analysis are used in order to check whether the motor parameters meet the expected specifications. The design steps are repeated in an iterative process until the design specifications are obtained.

3.2 Output equation

The LSRM design is addressed using two different approaches. In the first approach, it is performed in the rotary domain which is then transformed back into the linear domain [10, 11]. In the second approach, the LSRM design is carried out by using an analytical formulation of the average translation force determined by means of an idealized energy conversion loop [12, 13]. A design procedure for longitudinal flux flat LSRMs, based on this second approach, is proposed according the flowchart of shown in **Figure 5**, in which the average translation force, is determined in terms of magnetic loading, current density and geometrical relationships derived from a sensitivity analysis reported in [14]. Once the main dimensions are obtained, the number of turns per phase is determined by means of an iterative process.

The number of phases (m) and the pole stroke (PS) can be used to determine T_p, T_s, N_p, and N_s, by means of the following equations:

$$\left.\begin{aligned} N_P &= 2 \cdot m \\ N_S &= 2 \cdot (m \pm 1) \end{aligned}\right\} \tag{8}$$

$$\left.\begin{aligned} T_P &= \frac{1}{2} \cdot N_S \cdot PS = b_p + c_p \\ T_S &= \frac{1}{2} \cdot N_P \cdot PS = b_s + c_s \end{aligned}\right\} \tag{9}$$

The average internal electromagnetic force or translation force ($F_{x,avg}$) is calculated using an idealized nonlinear energy conversion loop in which the unaligned magnetization curve is assumed to be a straight line and the aligned magnetization curve is represented by two straight lines [13, 14]. This simplified model accounts for the saturation effect and is described in **Figure 6**. Assuming a flat-topped current waveform (hysteresis control), the area OACFO is the energy conversion area (W). Excluding iron and friction losses, the average translation force per phase ($F_{X,avg}$) is then obtained by

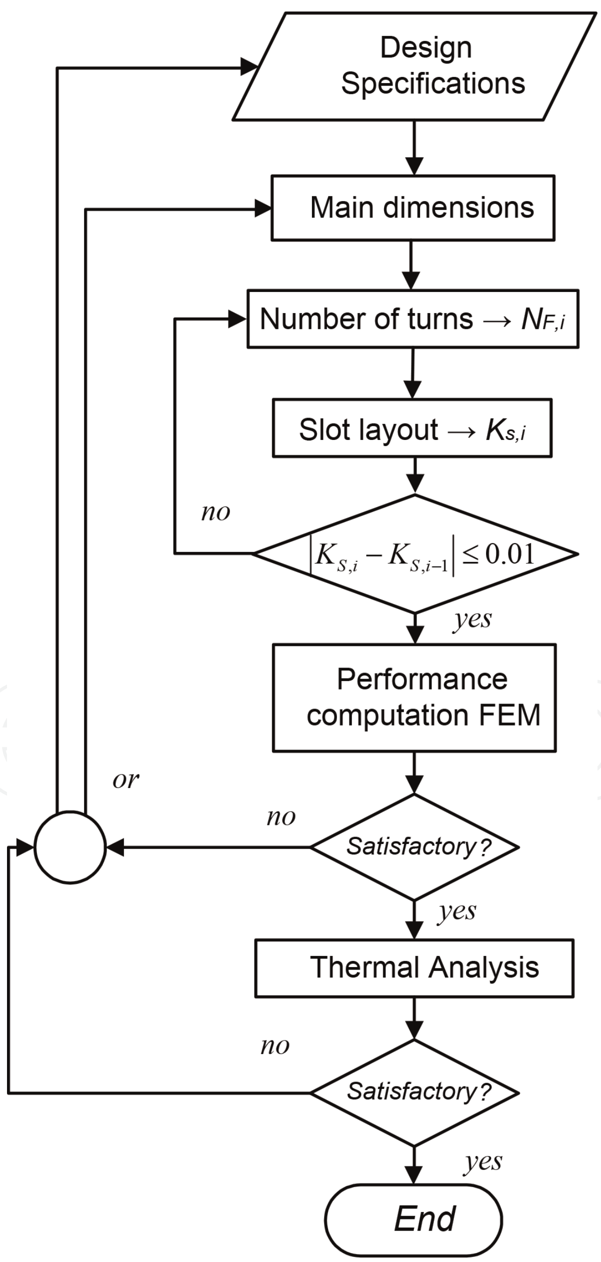

Figure 5.
Flowchart of the overall design procedure.

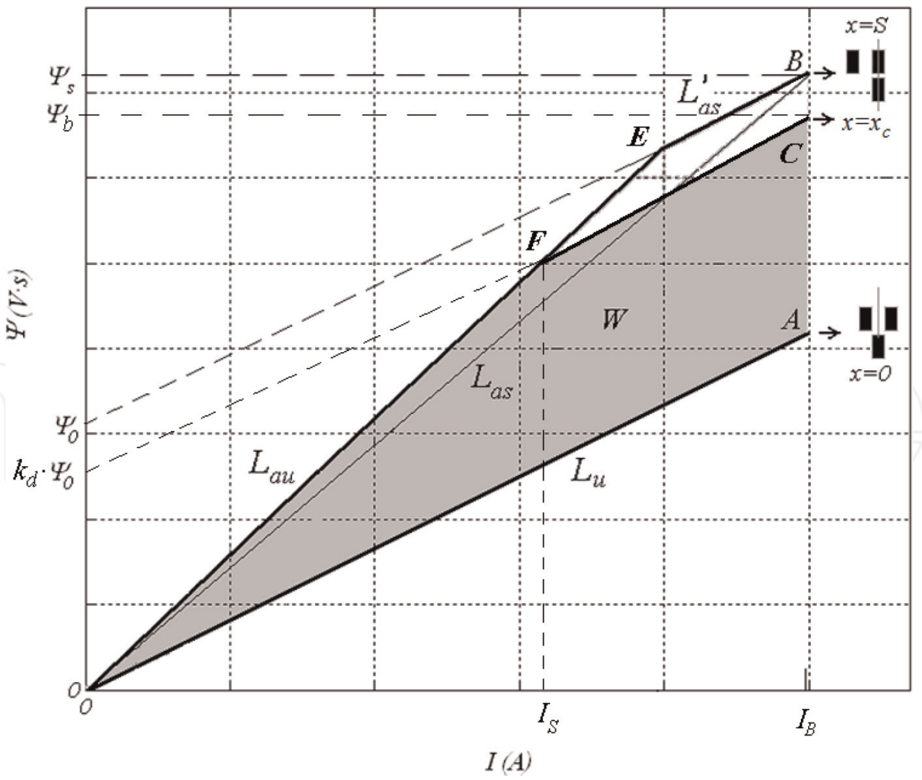

Figure 6.
Idealized nonlinear energy conversion loop.

$$F_{X,\,avg} = \frac{W}{S \cdot k_d} \tag{10}$$

where k_d is the magnetic duty cycle factor defined as $k_d = x_c/S$ (see **Figure 6**) and S is the distance between aligned and unaligned positions given by

$$S = \frac{T_s}{2} = \frac{N_p}{N_s} \cdot \frac{T_p}{2} \tag{11}$$

From **Figure 6** the following expressions can be derived:

$$W = I_B^2 \cdot L_{as} \cdot K_L \cdot k_d \tag{12}$$

where K_L is a dimensionless coefficient defined from the inductances depicted in **Figure 6**, by

$$K_L = \left(1 - \frac{L_u}{L_{as}}\right) \cdot \left(1 - \frac{1}{2} \cdot \frac{L_{as} - L_u}{L_{au} - L_u} \cdot k_d\right) \tag{13}$$

At point B (see **Figure 6**), the poles are fully aligned and therefore

$$\psi_s = L_{as} \cdot I_B = B_p \cdot N_1 \cdot N_{pp} \cdot b_p \cdot L_W \tag{14}$$

The total ampere-turns per slot ($N_1 \cdot I_B$) can be expressed, considering the slot fill factor (K_s) by means of the current density peak (J_B) by

$$N_1 \cdot I_B = \frac{1}{2} \cdot c_p \cdot l_p \cdot K_s \cdot J_B \tag{15}$$

Combining (15) and (16) into (13)

$$W = \frac{1}{2} \cdot (K_L \cdot K_s \cdot k_d) \cdot (c_p \cdot b_p \cdot l_p \cdot L_W \cdot N_{pp}) \cdot (B_p \cdot J_B) \quad (16)$$

Therefore, the average translation force per phase is

$$F_{X,\,avg} = N_{pp} \cdot \left(\frac{N_s}{N_p}\right) \cdot (K_L \cdot K_s) \cdot \left(\frac{c_p \cdot b_p \cdot l_p \cdot L_W}{T_P}\right) \cdot (B_p \cdot J_B) \quad (17)$$

In order to obtain dimensionless variables, the stator pole pitch (T_P) normalizes the geometric variables depicted in **Figure 4**, obtaining

$$\alpha_p = b_p/T_P \quad (18)$$

$$\alpha_s = b_s/T_P \quad (19)$$

$$\beta_p = l_p/T_P \quad (20)$$

$$\beta_s = l_s/T_P \quad (21)$$

$$\gamma_W = L_W/T_P \quad (22)$$

$$\delta_y = h_y/T_P \quad (23)$$

Rewriting (18) by considering (19)–(24)

$$F_{X,\,avg} = N_{pp} \cdot \left(\frac{N_s}{N_p}\right) \cdot (K_L \cdot K_s) \cdot \left(\left(\alpha_p - \alpha_p^2\right) \cdot \beta_p \cdot \gamma_W\right) \cdot T_P^3 \cdot (B_p \cdot J_B) \quad (24)$$

The output Eq. (25) is applicable to all the types of LSRMs considered in **Figure 1**, just considering N_{pp} = 2 for single-sided flat and tubular LSRMs and N_{pp} = 4 for conventional double-sided LSRMs and for modified double-sided LSRMs.

3.3 Selection of magnetic loading, current density and normalized geometric variables

The magnetic flux density in the stator pole (B_p) depends on the chosen magnetic lamination material; a good choice is to take a value slightly lower than the value at which laminations reach magnetic saturation. The current density, J_B, strongly depends on operation conditions and cooling facilities. The current density should be kept within reasonable margins if the temperature rise should not exceed a specified value. For high force LSRMs with air natural/forced convection and continuous duty cycle, J_B = 5 A/mm^2 is a good value while for the same conditions but following a short time intermittent duty cycle, J_B = 15 A/mm^2 could be more advisable.

The K_L coefficient depends on the geometrical parameters (see **Table 2**) and the current density (J_B). For values of current density between 5 and 20 A/mm^2, a good initial choice is K_L = 0.3.

The influence of the normalized geometric variables involved in the output equation as well as the current density has been investigated in [14]. **Table 2** shows the set of values of α_p and β_p, for different values of current density, recommended to obtain high values of average force [9].

The average force is proportional to L_W. However, an excessive stack length increases mass and iron losses. The air-gap length (g) should be as small as possible

J_B (A/mm^2)	α_p	β_p
5	[0.333, 0.417]	≤3.5
10	[0.375, 0.5]	≤3
15	[0.417, 0.542]	≤2.5
20	[0.458, 0.542]	≤2

Table 2.
Recommended values of α_p and β_p to obtain high average force.

to maximize the average force compatible with tolerances and manufacturing facilities; it is advisable to avoid air-gap lengths under 0.3 mm. In the case of double-sided, LSRM is very important in the assembly process ensure that the upper and the lower air gaps have the same length.

3.4 Number of turns and wire gauge

The maximum flux linkage at point B (see **Figure 6**), at a constant velocity, u_b, with a flat-topped current waveform and disregarding resistance, is related to the DC voltage V_b by means of

$$\psi_0 = \frac{V_b}{u_b} \cdot S \tag{25}$$

Thus

$$\psi_0 = \psi_s \cdot (1 - L_u/L_{as}) \tag{26}$$

Combining (26) and (27) into (15), the number of turns per pole is given by

$$N_1 = \frac{V_b \cdot S}{N_{pp} \cdot b_p \cdot L_W \cdot u_b \cdot B_p \cdot (1 - L_u/L_{as})} \tag{27}$$

The number of turns per phase is

$$N_F = N_{pp} \cdot N_1 \tag{28}$$

The way to obtain the number of turns is by means of an iterative process. This iterative process is shown in **Figure 7**, in which K_L = 0.3 and $N_1 = V_b \cdot S/(N_{pp} \cdot b_p \cdot L_W \cdot u_b \cdot B_p)$ are taken as initial conditions. Aligned (L_{au}) and unaligned (L_u) inductances can be computed by 2D FEM or by using classical magnetic circuit analysis based on lumped parameters, in both cases considering leakage pole flux and end-effects [15].

Initially, the slot fill factor (K_s) is unknown, so $K_{s,0}$ = 0.4 is a good starting point. Once the number of turns per pole and the wire gauge have been obtained, K_s should be recalculated again by means of

$$K_s = \frac{2 \cdot S_c \cdot N_1}{c_p \cdot l_p} \tag{29}$$

If the slot fill factor (K_S) obtained from (30) differs from its initial value plus an accepted error (see **Figure 5**), then the number of turns should be recalculated again taking as initial slot fill factor the last value obtained.

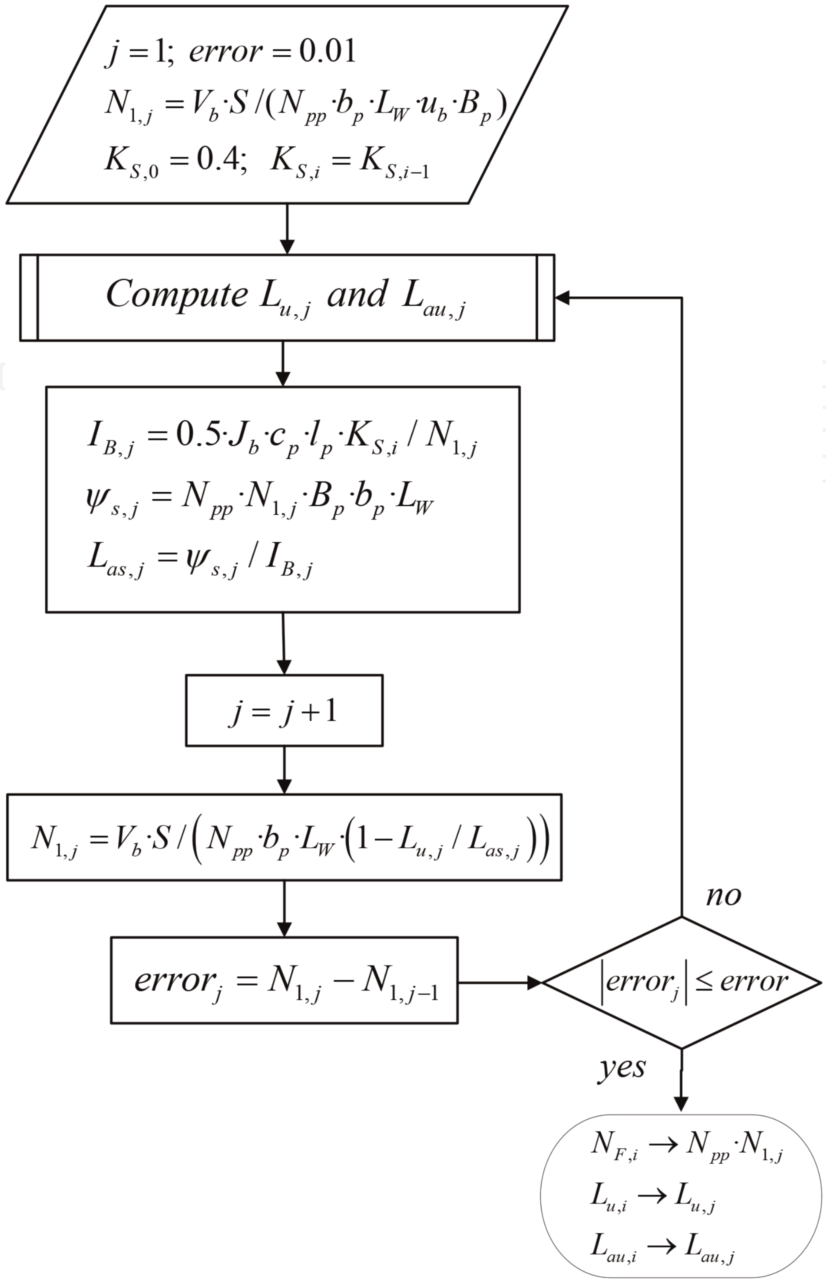

Figure 7.
Iterative process to obtain the number of turns per coil, N_1.

3.5 Finite element analysis

The best option to address the finite element analysis (FEA) process is to use three-dimensional 3D-FEA, but its use is discouraged because of the large computing time it could take. In order to overcome that handicap, it used a 2D-FEA adjusted in accordance with the end-effects. The end-effects in 2D FEA are considered by means of the end-effects coefficient, K_{ee} [16], given by:

$$\psi_{3D} = K_{ee} \cdot \psi_{2D} \tag{30}$$

$$L_{3D} = K_{ee} \cdot L_{2D} \tag{31}$$

where Ψ_{2D} and L_{2D} are the flux linkage and the inductance obtained by 2D-FEA; and Ψ_{3D} and L_{3D} are the 3D flux linkage and the inductance approach that account for the end-effects and are closer to the measured values. The correction factor K_{ee} is defined as [16, 17]

$$K_{ee} = \left(1 + \frac{L_{end} \cdot K_{si}}{L_{2D}}\right) \cdot K_f \tag{32}$$

where L_{end} is the end-winding inductance, K_{si} is a factor that affects L_{end} due to the steel imaging effect [17], and K_f is the axial fringing factor. K_{si} can usually be omitted (K_{si} = 1) since its effect on L_{end} is generally less than 2%. End-winding inductance, L_{end}, can be analytically deduced from end-winding geometry or can be computed by means of an axis-symmetrical 2D finite element model.

The co-energy (W'_{3D}), knowing (Ψ_{3D}), is calculated using the well-known expression:

$$W'_{3D}(x_i, I) = \int_o^I \psi_{3D}(x, i) \cdot di \Big|_{x_i = Ctn} \tag{33}$$

Then, the translation force, including end-effects, is obtained by

$$F_{x,\,3D}(x, I) = \frac{\partial W'_{3D}(x, I)}{\partial x}\Big|_{I = Ctn} \tag{34}$$

In order to offer a practical formulation of (34), it can be rewritten in (35)

$$F_{x,\,3D}(x, I_B) \approx \frac{\Delta W'_{3D}}{\Delta x} = \frac{\Delta I}{\Delta x} \cdot \left[\sum_0^{I_B} \psi_{3D}(x + \Delta x, I) - \sum_0^{I_B} \psi_{3D}(x, I)\right] \tag{35}$$

3.6 Thermal analysis

The objective of this analysis is to check that, within the specified conditions of operation, the temperature rise in the different parts of the LSRM does not surpass the limit value of the chosen insulation class. Thermal analyses of electric rotating machines have been extensively described in the literature [18–26], but up to now little attention has been paid to the thermal analysis of LSRMs [22]. Thermal analyses can be conducted by means of analytical or numerical methods. The analytical method based on lumped parameters is faster, but its accuracy depends on the level of refinement of the thermal network and on the knowledge of the heat transfer coefficients. In this paper a lumped parameter thermal model adapted to the LSRM is used in which the heat transfer coefficients are estimated taking into account previous studies in rotating machines [23–25].

3.7 Design verification

In order to verify the described design procedure, a four-phase double-sided LSRM prototype has been designed, built, and tested. Its main design specifications and its main dimensions, obtained following the proposed design procedure, are shown in the Appendix (**Table 4**).

3.7.1 Finite element verification

The finite element analysis is carried out by means of a 2D-FEM solver. The magnitudes computed are the 2D linked flux $\psi_{2D}(x, i)$, for a set of evenly distributed current ($0 \div I_B$), and positions between alignment and nonalignment, in **Figure 8** the flux density plots for the aligned (see **Figure 8a**) and nonaligned positions (see **Figure 8b**) for the LSRM prototype are shown.

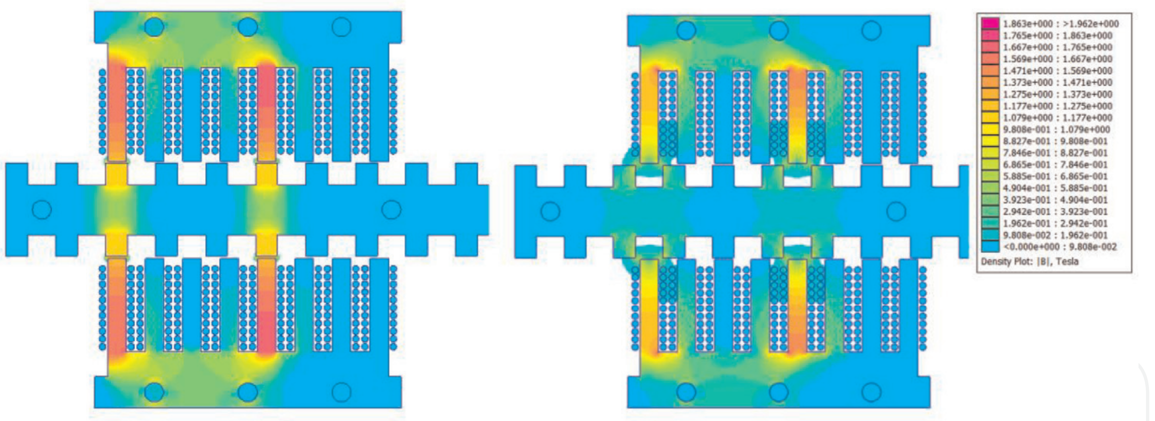

Figure 8.
Flux density plots from 2D FEA of the four-phase LSRM (a) aligned x = 0. (b) Unaligned x = S.

In order to verify and compare the results, the prototype was analyzed by means of the finite element method (FEM) described in Section 3.5 adapted to account for end-effects. The values of static force were also obtained experimentally using a load cell UTICELL 240. The measured and FEM computed force results are shown in **Figure 9**. Finally, the results for the average static force obtained by experimental means and by FEM are compiled in **Table 3**.

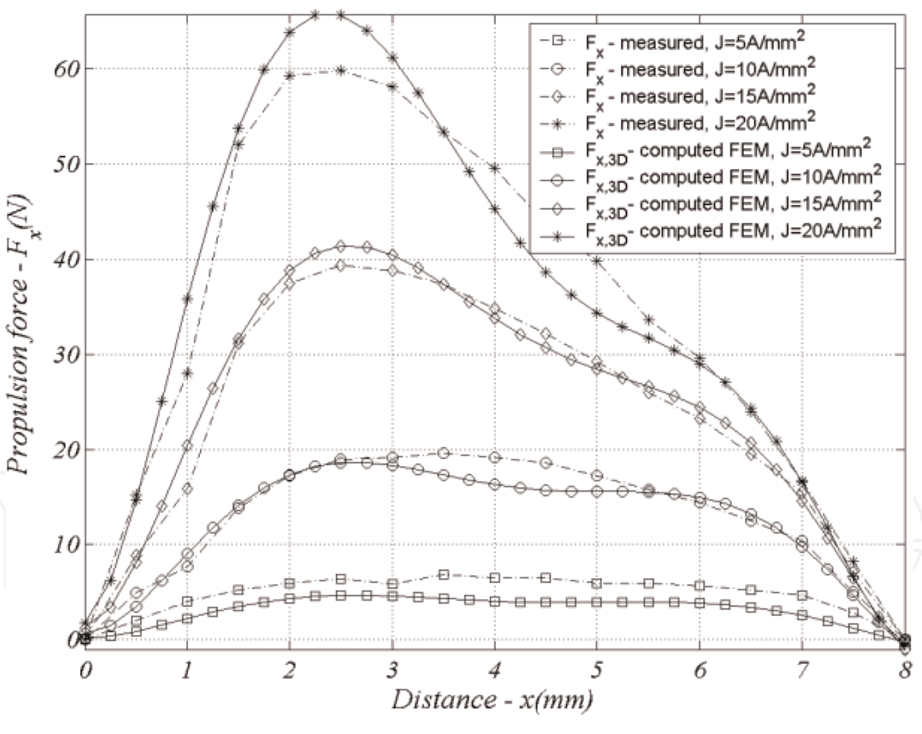

Figure 9.
Static force $F_x(J,x)$. Comparison of results.

J_B = 15 A/mm^2	$F_{x,avg}$ (N)
Measured	23.3
FEM	24.5

Table 3.
Average static force comparison of results.

3.7.2 Thermal verification

The lumped parameter thermal model mentioned in Section 3.6 and explained in depth in [26] was applied to our case study. The location of the nodes in the cross section of the double-sided flat LSRM prototype is shown in **Figure 10**, and the completed lumped thermal model is depicted in the circuit of **Figure 11**. The temperature rise over ambient temperature in each node was obtained solving the thermal network with *MATLAB-Simulink*. **Figure 12** shows the simulated and experimental results of a heating test consisting on feeding a phase with DC current at 15 A/mm^2 for a period of 1800 s and after that a cooling period of 1800 s by natural convention. The time evolution of temperature in node 4 (critical node) is compared with a platinum resistance thermometer sensor (PT100) placed in the same point.

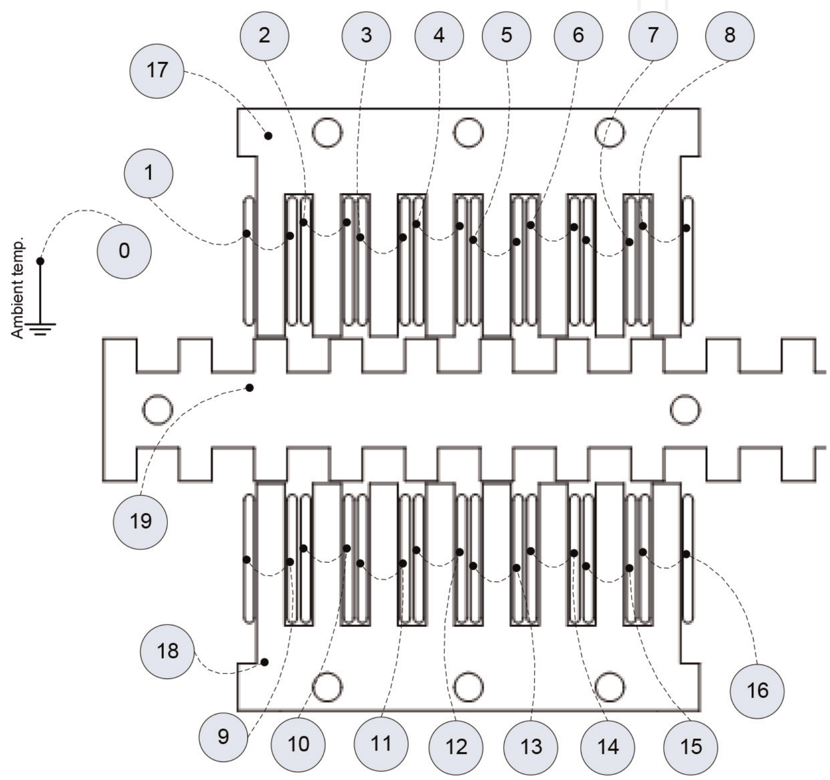

Figure 10.
Cross section of double-sided LSRM prototype showing node location.

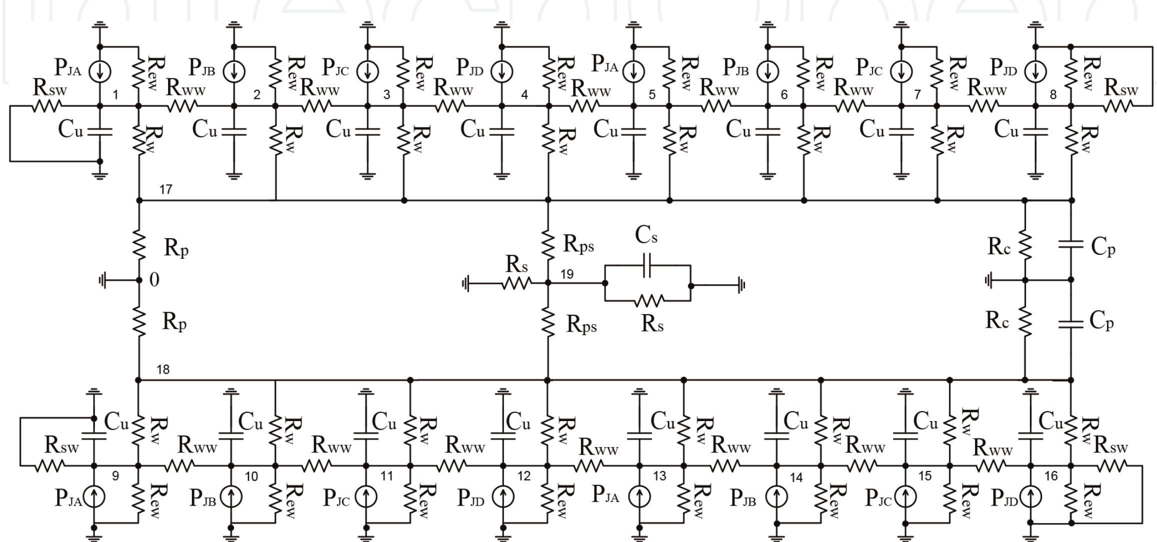

Figure 11.
Lumped-parameter thermal model for the double-sided LSRM prototype.

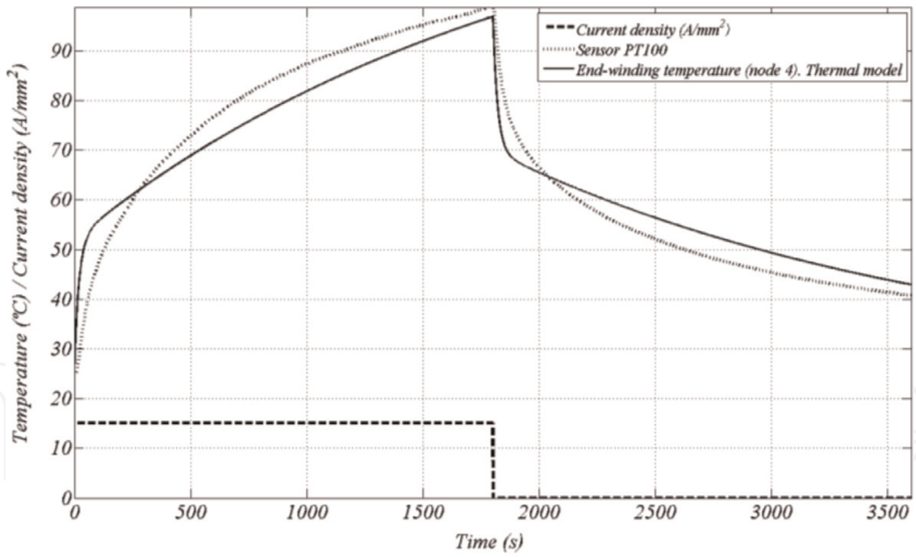

Figure 12.
Comparison of temperature rise results in node 4, for the LSRM prototype.

3.8 Discussion of results

Once built and tested, the prototype of double-sided LSRM is appropriate to proceed with a discussion of the results. It can be observed (**Figure 9**) that the static force results obtained by 2D-FEA, adjusted to take into account end-effects, are in good agreement with those measured experimentally except for those corresponding to high values of current density (20 A/mm^2), values that are outside the scope of application of the designed LSRM. The average static force values, for a current density of 15 A/mm^2, obtained by measurements are very close with those results of simulation by FEA (**Table 3**). The comparison of temperature raises results for node 4, in which a sensor of temperature was placed, between the values obtained using the proposed thermal model, and the experimental values measured by means of a sensor PT100 are quite good, but they also show that it would be advisable to improve the model, increasing the level of refinement of the thermal network. Anyway, the comparison between computed and experimental results is enough and good to validate the proposed design procedure.

4. Simulation model and experimental results of an LSRM actuator

The simulation of an LSRM force actuator is presented [27]. This linear actuator is formed by a longitudinal flux double-sided LSRM of four phases that has been designed following the design procedure before being described, and of which the main characteristics are given in the Appendix (**Table 4**). It is fed by an electronic power converter, an asymmetric bridge with two power MOSFETs switches and two diodes per phase, which incorporate drivers, snubbers, and current transducer for each phase. An optical linear encoder designed for this purpose, composed by four optical switches (S1, S2, S3, S4) is used in order to know the position at any time. The actuator is controlled by a digital force controller. The LSRM force actuator simulation model has been implemented in *MATLAB-Simulink*.

The simulation block diagram is shown in **Figure 13**, and it consists of three blocs: the power converter block, the LSRM motor block, and the digital control block.

The electronic power converter is implemented in *MATLAB-Simulink* by means of the *SimPowerSystems* toolbox. This block needs the previous knowledge of the gate signals which are generated by the switching signals module of the digital control block.

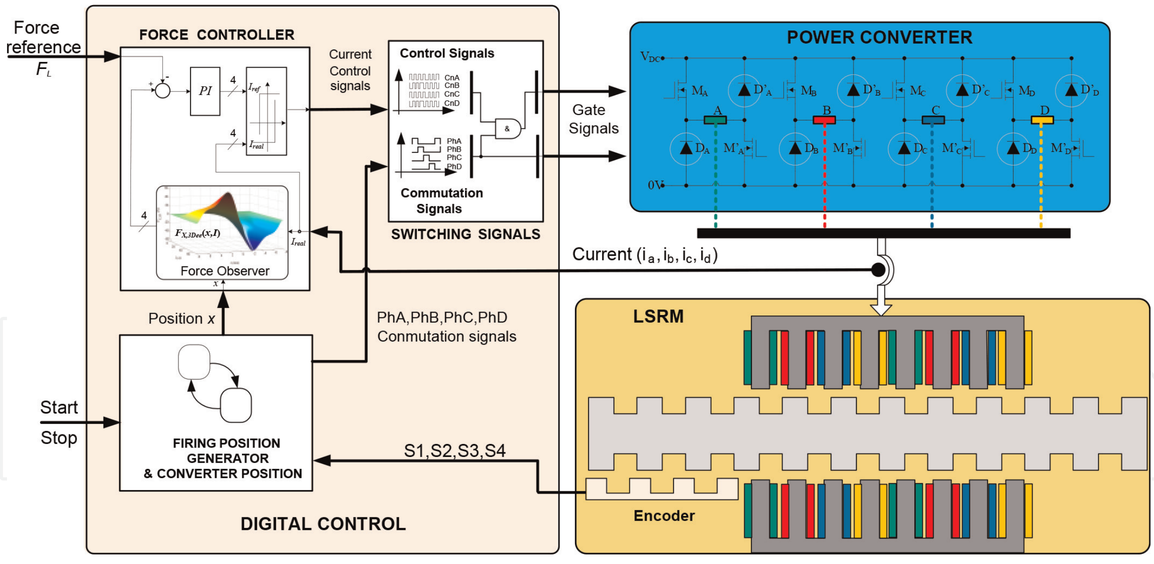

Figure 13.
LSRM force actuator simulation block diagram.

The LSRM block has to solve the mathematical model of the SRM, i.e., the space-state equations (7). To solve the instantaneous phase current (8), it is needed to know the phase voltages, the partial derivatives of the flux (lookup tables), and the phase resistance (**Figure 14**). The optical switch signals are obtained from integrating the speed of the mechanical equation (8), generating a Boolean set of digital signals in order to produce the phase activation sequence shown in **Figure 15**.

The force control block implements a PI controller and a hysteresis loop for generating the current control signals. The force is estimated using a force-observer which consists in a lookup table (static force curves of LSRM), previously computed using the 2D FE procedure described in Section 3.5, and therefore, the knowledge of phase currents (i_a, i_b, i_c, i_d) and of the position (x) is required. The phase currents are directly obtained from the electronic power converter output, and the position is from the firing position generator module of the digital control block. A hysteresis

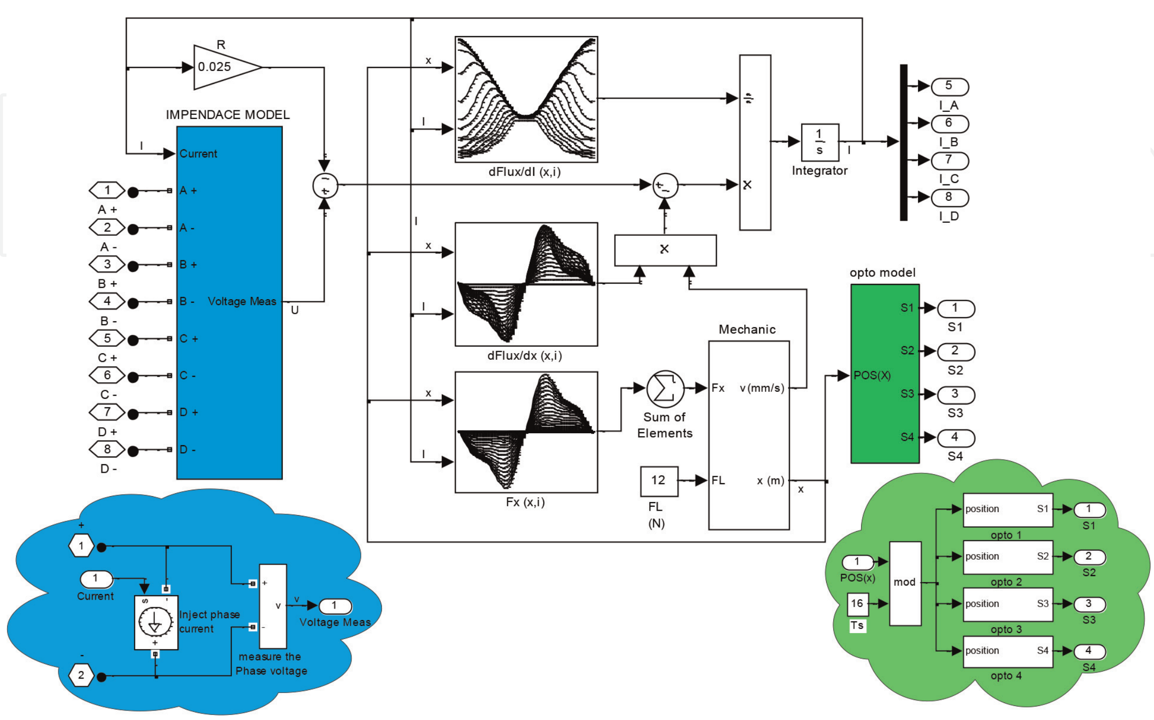

Figure 14.
LSRM, load and opto-switches Simulink model.

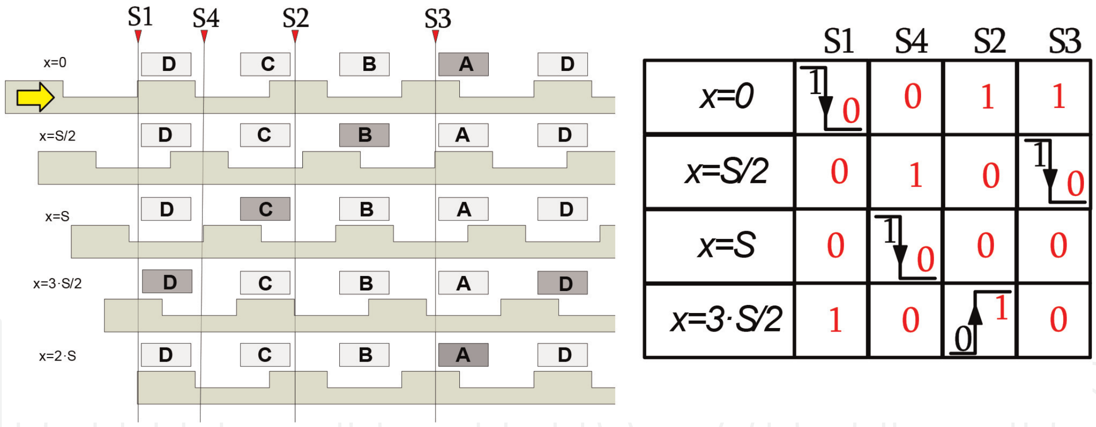

Figure 15.
Encoder: phase activation sequence.

control adjusts the translation force to a given reference force (F_L). The program adjusts the frequency of the gate control signals of the MOSFET in order to match to the required force. The force control is implemented by means of a DSPACE ACE kit 1006 (**Figure 16**).

The simulation results are presented in **Figure 17**. The conducting interval is equal to the pole stroke, which is 4 mm in all the cases. In **Figure 17**, it can also be shown the influence of the firing position (x_1) over the current waveform. When firing at x_1 = 0 mm, the electromagnetic force $F_{x,\,3D}(x, i)$ is zero at the beginning of the conduction interval (see **Figure 17a**), and a current peak appears near this position. Firing at x_1 = 1 mm and x_1 = 2 mm, the resulting conduction intervals are from 1 to 5 mm and from 2 to 6 mm, respectively. In these intervals is where the force reaches the maximum values, which produces a current waveform almost flat. When the firing position is at x_1 = 3 mm, the conduction interval is from 3 to 7 mm, and a current peak appears at the end of the period because the electromagnetic force at x = 7 mm is quite low (is 0 at x = 8 mm), and therefore, a high increasing in current is required to maintain the force constant. In conclusion, firing near aligned (x = 0 mm) and unaligned (x = 8 mm) positions at low speed produces high current peaks, which is not advisable.

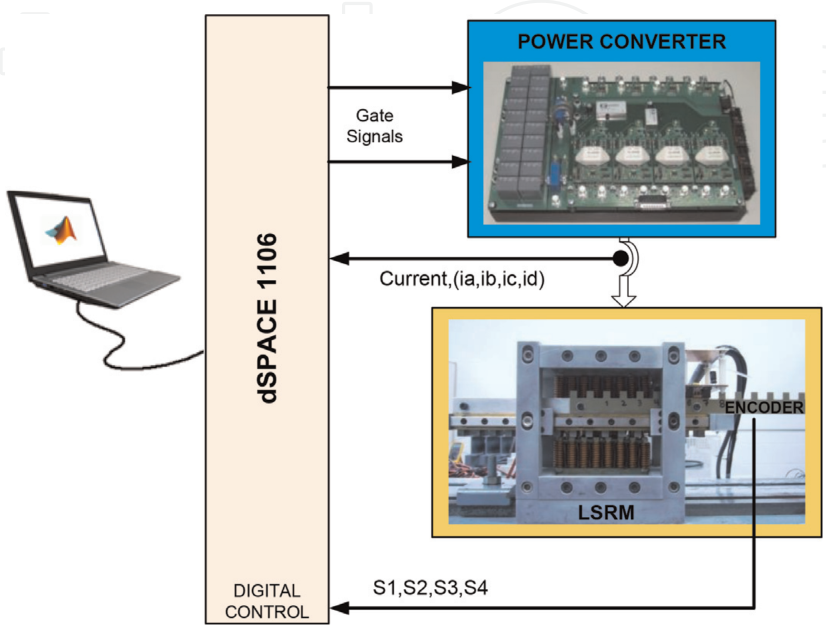

Figure 16.
LSRM force actuator hardware implementation.

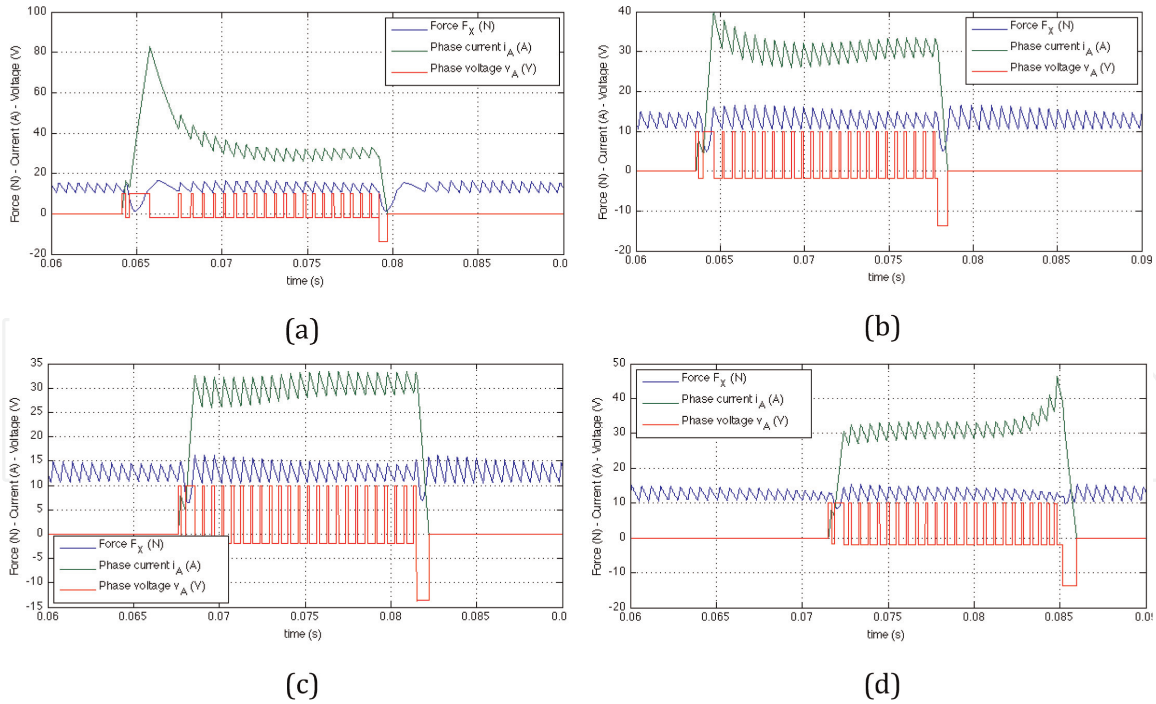

Figure 17.
Simulation results for different turn on (x_1) positions. (a) x_1 = 0 mm; (b) x_1 = 1 mm; (c) x_1 = 2 mm; and (d) x_1 = 3 mm.

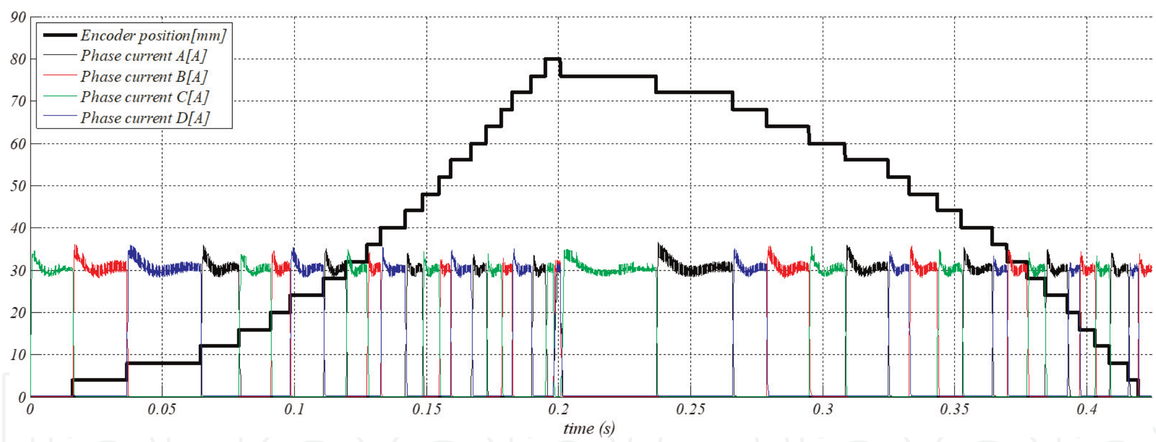

Figure 18.
Measured position and measured phase currents at turn on x_1 = 1 mm.

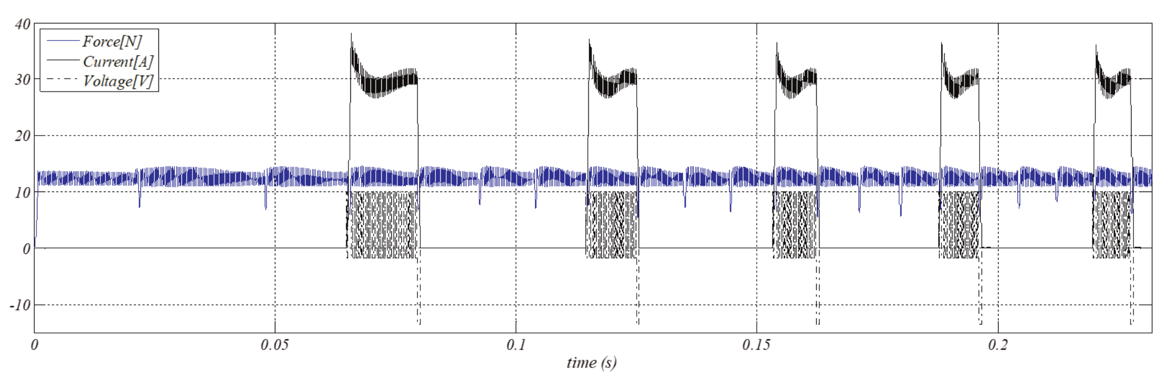

Figure 19.
Measured phase-a results during acceleration at turn on x_1 = 1 mm.

Figures 18 and **19** show the experimental results obtained from the four-phase LSRM which are shown in **Figure 16**. The experimental results display a good agreement with simulation results. The mover stroke is 80 mm, and this distance is covered in 0.2 s, which gives an average speed of 0.4 m/s.

5. Conclusion

In this chapter, after the presentation of a mathematical model of the LSRM, a design methodology for LSRM is proposed. This methodology is based on an analytical formulation of the average translation force determined using a nonlinear energy conversion loop. The main dimensions of the LSRM were determined from machine specifications, the aforementioned average translation force formula, and geometric relationships. 2D finite element analysis, corrected to take into account end-effects, and lumped parameter thermal analysis were used to refine and/or to validate the proposed design. An LSRM prototype was built following the described design approach that was validated by experimental results. Then, modeling and simulation of an LSRM force actuator are presented. This linear actuator is formed by the LSRM prototype, by an electronic power converter with two power MOSFET switches and two diodes per phase, incorporating drivers, snubbers, and current transducers for each phase and by an original, simple, and low-cost optical linear encoder designed for this purpose, composed of four optical switches. The actuator is controlled by a digital force controller that is implemented by means of a PI controller and a hysteresis loop for generating the current control signals. The force is estimated using a force-observer which consists in a lookup table previously computed using the 2D finite element analysis. The LSRM force actuator simulation model was implemented in MATLAB-Simulink. Experimental results were in good agreement with simulations and confirmed that the proposed LSRM actuator as an alternative to pneumatic actuators or of the assembly of AC servomotors coupled to a timing belt or a ball screw for injection molding machines.

Conflict of interest

The authors declare no conflict of interest.

Nomenclature

a	acceleration (m/s^2)
b_p	primary pole width (m)
B_p	magnetic flux density in the active pole (T)
b_s	secondary pole width (m)
c_p	primary slot width (m)
c_s	secondary slot width (m)
$e_{m,j}$	back electromotive force (V)
F_x	translation force, internal electromagnetic force (N)
F_r	friction force (N)
F_L	load force (N)
g	air-gap length (m)
h_{yp}	primary yoke height (m)
h_{ys}	secondary yoke height (m)
I_B	flat-topped current peak (A)

i_j current phase j (A)
J_B current density peak (A/m^2)
k_d magnetic duty cycle factor
K_s slot fill factor
L_{au} unsaturated aligned inductance (H)
L_{as} saturated aligned inductance (H)
L'_{as} saturated aligned incremental inductance (H)
L_{end} end-winding inductance (H)
l_p primary pole length (m)
l_s secondary pole length (m)
L_j incremental inductance (H)
L_u unaligned inductance (H)
L_W stack length (m)
m number of phases
M mass of the mover (m_t) plus the payload (m_l)
n number of switching devices per phase
N_1 number of coils per pole
N_p number of active poles per side (primary)
N_{pp} number of active poles per phase
N_s number of passive poles per side (secondary)
PS stroke (m)
R phase resistance (Ω)
S distance between aligned and unaligned positions (m)
S_c cross section of the wire (m^2)
T_p primary pole pitch (m)
T_s secondary pole pitch (m)
TS mover stroke (m)
u_b velocity (m/s)
u_j voltage phase j (V)
V_b DC bus voltage (V)
W energy conversion loop (J)
x mover position (m)
x_c turn-off current position (m)
ψ flux linkage (Wb)

Appendix

Specifications		
Rated force	F_X	25 N
Number of phases	m	4
Lamination steel	M-19 (B_{sat} = 1.8 T)	
DC Bus voltage	V_b	12 V
Temperature rise (class F)	ΔT	100°C
Dimensions		
Pole stroke	PS	4 mm
Primary pole width	b_p	6 mm
Primary slot width	c_p	6 mm
Primary pole pitch	T_p	12 mm

Number of active poles per side	N_p	8
Primary pole length	l_p	30 mm
Secondary pole width	b_s	7 mm
Secondary slot width	c_s	9 mm
Secondary pole pitch	T_s	16 mm
Number of passive poles per side	N_s	6
Secondary pole length	l_s	7 mm
Yoke length	h_y	8 mm
Stack length	L_W	30 mm
Number of turns per pole	N_1	11
Wire diameter	d_c	2.1 mm
Air-gap length	g	0.5 mm

Table 4.
LSRM prototype main dimensions.

Author details

Jordi Garcia-Amoros[1]*, Pere Andrada[2] and Baldui Blanque[2]

1 Electrical Engineering Department (DEEEA), Universitat Rovira i Virgili, Tarragona, Spain

2 GAECE, Electric Engineering Department, Universitat Politècnica de Catalunya, BARCELONATECH, EPSEVG, Vilanova i la Geltrú, Spain

*Address all correspondence to: jordi.garcia-amoros@urv.cat

References

[1] Bianchi N, Bolognani S, Corda J. Tubular linear motors: A comparison of brushless PM and SR motors. In: International Conference on Power Electronics, Machines and Drives (Conf. Publ. No. 487); June 4–7, 2002; pp. 626-631. DOI: 10.1049/cp:20020189

[2] Zhao SW, Cheung NC, Gan W-C, Yang JM, Pan JF. A self-tuning regulator for the high-precision position control of a linear switched reluctance motor. IEEE Transactions on Industrial Electronics. 2007;**54**(5):2425-2434. DOI: 10.1109/TIE.2007.900348

[3] Kolomeitsev L, Kraynov D, Pakhomin F, Kallenbach E, Kireev V, Schneider T, et al. Linear switched reluctance motor as high efficiency propulsion system for railway vehicles. In: SPEEDAM 2008; 2008. pp 155-160. DOI: 10.1109/EPEPEMC.2008.4635495

[4] Lobo NS, Lim HS, Krishnan R. Comparison of linear switched reluctance machines for vertical propulsion application: Analysis, design, and experimental correlation. IEEE Transactions on Industry Applications. 2008;**44**(4):1134-1142. DOI: 10.1109/TIA.2008.926294

[5] Zhu Z, Cheung NC, Cheng KWE, Xue X, Lin J. Direct instantaneous force control with improved efficiency for four-quadrant operation of linear switched reluctance actuator in active suspension system. IEEE Transactions on Vehicular Technology. 2012;**61**(4):1567-1576. DOI: 10.1109/IWECMS.2011.5952367

[6] Llibre J-F, Martinez N, Nogarede B, Leprince P. Linear tubular switched reluctance motor for heart assistance circulatory: Analytical and finite element modeling. In: 10th International Workshop on Electronics, Control, Measurement and Signals (ECMS); June 1–3, 2011. pp. 1-6

[7] Du J, Liang D, Xu L, et al. Modeling of a linear switched reluctance machine and drive for wave energy conversion using matrix and tensor approach. IEEE Transactions on Magnetics. 2010;**46**(6):1334-1337. DOI: 10.1109/TMAG.2010.2041041

[8] Garcia Amorós J. Aportaciones al diseño y caracterización del motor lineal de reluctancia autoconmutada [PhD thesis]. Vilanova i la Geltrú (Barcelona): UPC BarcelonaTech; 2010. Available from: http://hdl.handle.net/2117/94579

[9] Garcia-Amoros J, Andrada P, Blanqué B. Design procedure for a longitudinal flux flat linear switched reluctance motor. Electric Power Components & Systems. 2010;**40**(2):161-178. DOI: 10.1080/15325008.2011.629333.

[10] Byeong-Seok L, Han-Kyung B, Praveen V, Krishnan R. Design of a linear switched reluctance machine. IEEE Transactions on Industry Applications. 2000;**36**(6):1571-1580. DOI: 10.1109/28.887208

[11] Krishnan R. Switched Reluctance Motor Drives. Modeling, Simulation, Analysis, Design and Applications. Boca Raton: CRC Press; 2001. DOI: 10.1201/9781420041644

[12] Boldea I, Nasar SA. Linear Electric Actuators and Generators. Cambridge: Cambridge University Press; 1997. DOI: 10.1017/CBO9780511529641

[13] Miller TJE. Converter volt-ampere requirements of the switched reluctance motor drive. IEEE Transactions on Industry Applications. 1985;**21**(5):1136-1144. DOI: 10.1109/TIA.1985.349516

[14] Amorós JG, Andrada P. Sensitivity analysis of geometrical parameters on a double-sided linear switched reluctance

motor. IEEE Transactions on Industrial Electronics. 2010;**57**(1):311-319. DOI: 10.1109/TIE.2009.2032208

[15] Amorós JG, Andrada P. Magnetic circuit analysis of a linear switched reluctance motor. In: Proceedings of the 13th European Conference on Power Electronics and Applications (EPE 2009); Barcelona, Spain; 2009

[16] D'hulster F, Stockman K, Belmans RJM. Modelling of switched reluctance machines: State of the art. International Journal of Modelling and Simulation. 2004;**24**(4):216-223. DOI: 10.1080/02286203.2004.11442306

[17] Matveev A, Kuzmichev V, Lomonova E. A new comprehensive approach to estimation of end-effects in switched reluctance motors. In: Proceedings of XV International Conference on Electrical Machines (ICEM 2002); Bruges, Belgium; 2002

[18] Srinivas KN, Arumugam R. Thermal characterization through finite element analysis of the switched reluctance motor. In: Proceedings of IEEE Region 10 International Conference on Electrical and Electronic Technology (TENCON 2001). Vol. 2; Singapore; 2001. pp. 819-823. DOI: 10.1109/TENCON.2001.949707

[19] Mellor PH, Roberts D, Turner DR. Lumped parameter thermal model for electrical machines of TEFC design. Proceedings of the Institution of Electrical Engineers - Part B: Electric Power Applications. 1991;**138**(5): 205-218. DOI: 10.1049/ip-b.1991.0025

[20] Nerg M, Rilla M, Pyrhönen J. Thermal analysis of a radial-flux electrical machines with a high power density. IEEE Transactions on Industrial Electronics. 2008;**55**(10):3543-3554. DOI: 10.1109/TIE.2008.927403

[21] Staton D, Boglietti A, Cavagnino A. Solving the more difficult aspects of electric motor thermal analysis in small and medium size industrial induction motors. IEEE Transactions on Energy Conversion. 2005;**20**(3):620-628. DOI: 10.1109/IEMDC.2003.1210320

[22] Chayopitak N, Taylor DG. Thermal analysis of linear variable reluctance motor for manufacturing automation applications. In: Proceedings of IEEE International Conference on Electric Machines and Drives (IEMDC 2005); San Antonio, USA; 2005. pp. 866-873. DOI: 10.1109/IEMDC.2005.195824

[23] Boglietti A, Cavagnino A, Staton D. Determination of critical parameters in electrical machine thermal models. In: Conference Record of the Proceedings of 42nd IAS Annual Meeting; New Orleans, USA; 2007. pp. 73-80. DOI 10.1109/07IAS.2007.60

[24] Boglietti A, Cavagnino A, Staton D. Determination of critical parameters in electrical machine thermal models. IEEE Transactions on Industry Applications. 2008;**44**(4):1150-1159. DOI: 10.1109/TIA.2008.926233

[25] Staton D, Cavagnino A. Convection heat transfer and flow calculations suitable for electric machines thermal models. IEEE Transactions on Industrial Electronics. 2008;**55**(10):3509-3516. DOI: 10.1109/TIE.2008.922604

[26] Amorós JG, Andrada P, Blanqué B. An analytical approach to the thermal design of a double-sided linear switched reluctance motor. In: Proceedings of XIX International Conference on Electrical Machines (ICEM 2010); Rome, Italy; 2010. DOI: 10.1109/ICELMACH.2010.5608298

[27] Amorós JG, Blanque B, Andrada P. Modelling and simulation of a linear switched reluctance force actuator. IET Electric Power Applications. 2013;**7**(5): 350-359. DOI: 10.1049/iet-epa.2012.0391